Nanowire Heterostructures Comprising Germanium Stems and Silicon Branches as High-Capacity Li-Ion Anodes with Tunable Rate Capability

Tadhg Kennedy,[†,‡] Michael Bezuidenhout,[†,‡] Kumaranand Palaniappan,[†,‡] Killian Stokes,[†,‡] Michael Brandon,[†,‡] and Kevin M. Ryan*[,†,‡]

[†]Materials and Surface Science Institute, and [‡]Department of Chemical and Environmental Sciences, University of Limerick, Limerick, Ireland

ABSTRACT Here we report the rational design of a high-capacity Li-ion anode material comprising Ge nanowires with Si branches. The unique structure provides an electrode material with tunable properties, allowing the performance to be tailored for either high capacity or high rate capability by controlling the mass ratio of Si to Ge. The binder free Si—Ge branched nanowire heterostructures are grown directly from the current collector and exhibit high capacities of up to ~1800 mAh/g. Rate capability testing revealed that increasing the Ge content within the material boosted the performance of the anode at fast cycling rates, whereas a higher Si content was optimal at slower rates of charge and discharge. Using *ex-situ* electron microscopy, Raman spectroscopy and energy dispersive X-ray spectroscopy mapping, the composition of the material is shown to be transient in nature, transforming from a heterostructure to a Si—Ge alloy as a consequence of repeated lithiation and delithiation.

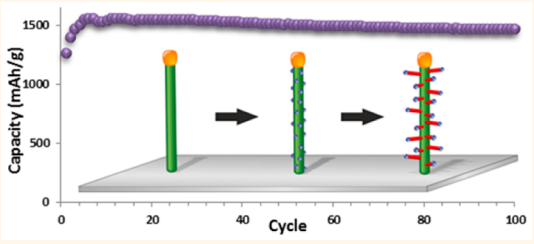

KEYWORDS: silicon · germanium · branched nanowires · heterostructure · lithium-ion anode

The ever increasing demand for portable electronic devices and the rapidly expanding electric vehicle market has fuelled the search for high-capacity electrode materials that can increase the energy density of lithium-ion batteries. Li-alloying materials such as Si and Ge have emerged as the forerunners to replace the current, relatively low-capacity carbonaceous based anodes.[1−5] As a result of the Li-rich binary alloys it forms upon charging, Si has the highest known gravimetric capacity (3579 mAh/g), almost 10 times that of the state-of-the-art graphitic-based materials. However, the large volume change associated with the formation of these alloys leads to structural degradation of the material and loss of contact from the current collector, ultimately limiting their cycle life. In an attempt to overcome this problem, nanowire (NW) based arrangements have been utilized with some success.[6−14] When grown directly from the current collector, the NW morphology outperforms bulk materials as each individual NW remains electrically contacted, despite the large volume fluctuations occurring as a result of constant alloying and dealloying. The ease of processability and uncomplicated, binder-free nature of such electrodes make them highly attractive as next-generation Li-ion anode materials. The seminal study on binder-free Si NW electrodes by Chan et al. demonstrated a stable and very high-capacity of 3200 mAh/g after 10 cycles.[6] In an attempt to extend the cycle life, more complex binder-free NW arrangements have been introduced such as carbon—silicon and crystalline—amorphous core—shell structures,[15,16] NWs coated with conductive inactive materials[17,18] and NWs grown via AAO template assisted growth.[19] Although all of these systems show some improvements in capacity retention, they suffer from the same major disadvantage of all Si electrodes, that of a relatively poor rate capability due to the inherently low conductivity of Si, slow rates of Li^+ diffusivity and incomplete lithiation of the material at high charge rates.[20−25] Ge NW electrodes on the other hand show a much superior rate capability due to the high conductivity (10 000× that of Si) and high rate of

* Address correspondence to kevin.m.ryan@ul.ie.

Received for review April 27, 2015 and accepted June 30, 2015.

Published online June 30, 2015
10.1021/acsnano.5b02528

diffusivity of Li (400× that of Si) making them suitable for high-rate applications.[26,27] Recently we demonstrated the stable cycling of Ge NWs grown directly from stainless steel (SS), displaying capacities in excess of 400 mAh/g even at very high discharge rates of up to 100C. Furthermore, these Ge NW electrodes exhibited high capacities (~900 mAh/g) and very long cycle lives (~2000 cycles) in long-term cycling experiments at rates of 1C.[28,29] The low capacity fade of these electrodes is due to the transformation of the NWs over the initial cycles into a spongelike network of Ge ligaments which remains well contacted to the current collector despite the volume changes occurring. This transformation is advantageous as the network is mechanically robust and highly stable leading to a very long cycle life with minimal capacity fade. However, the high cost of Ge due to its low abundance remains an obstacle for such electrodes. Incorporating a more inexpensive material such as Si into this stable network architecture would alleviate this problem while also providing the additional benefit of an overall increased gravimetric capacity. One possible route to this would be to grow a mixture of Ge and Si NWs directly from the same substrate; although this task is not trivial for chemical vapor deposition systems as it requires a seed material exclusive to either Ge NW or Si NW synthesis, and such a material, to the best of our knowledge, does not exist.[30] A more readily achievable design is a stem-branch type heterostructure consisting of a Ge stem contacted directly to the current collector with Si branches growing from it. In this arrangement, the porous network architecture formed through cycling could act as a support structure for Si, combining the excellent rate characteristics and capacity retention of Ge with the high capacity and lower cost of Si.

Here, we demonstrate stable cycling of a unique Si–Ge heterostructure consisting of Si NW branches growing from a Ge stem. By controlling the Ge to Si mass ratio within the material, the electrochemical characteristics of the electrodes can be tailored for either high capacity or high rate capability applications. Three different Ge to Si mass ratios were studied (2:1, 3:1, and 4:1) with the most Si rich electrode displaying the highest capacity (~1800 mAh/g) and the most Ge rich electrode displaying the best rate capability (~800 mAh/g when cycled at the very high rate of 10C). The Ge NWs were synthesized using a rapid, solvent-free protocol, with Si NW branch growth occurring via a secondary seeding method using Sn nanoparticles (NPs). The effect of cycling on the branched NWs was investigated using *ex situ* high-resolution transmission electron microscopy (HRTEM) and high-resolution scanning electron microscopy (HRSEM) and showed that the material restructured into a porous network of ligaments of active material. Furthermore, Raman spectroscopy revealed that, during this restructuring process, the active material transforms from a Si–Ge heterostructure into a Si–Ge alloy as a consequence of repeated lithiation and delithiation.

RESULTS AND DISCUSSION

Material Synthesis and Characterization. A schematic of the reaction setup for Ge NW growth is outlined in Figure 1a. A stainless steel current collector with a 1 nm thick evaporated layer of Cu on its surface is placed upright onto a preheated substrate (430 °C) in an inert atmosphere. A specially designed stainless steel confiner[31] is placed over the substrate to prevent the escape of the germanium precursor vapor, diphenylgermane, over the course of the reaction. The precursor is delivered to the substrate by means of an injection using a microliter syringe through a small hole in the top of the confiner. Discrete Cu_3Ge nanoparticle seeds are formed *in situ* and facilitate Ge NW growth via the well-known vapor–solid–solid (VSS) mechanism.[29] This system provides advantages over more conventional Ge NW synthesis routes such as chemical vapor deposition as it is inexpensive and affords rapid processing times with high density Ge NW growth achievable in reaction times as short as 30 s. A typical SEM image of the as synthesized Ge NWs is shown in Figure 2a with a higher resolution image of an individual NW shown in Figure 2b. The NWs exhibit two distinct morphological forms. The majority of the NWs have a tortuous, wormlike appearance with an average diameter of 74 nm. The remainder of the NWs are straight with a narrower average diameter of 39 nm. Dense NW growth is achieved across the entire substrate as evidenced by low magnification SEM images presented in the Supporting Information (Figure S1).

Growth of the Si branches from the surface of the Ge NWs was achieved via a secondary seeding step, utilizing Sn NPs as seeds for Si NW growth (Figure 1b). The Sn NPs were synthesized using a previously reported procedure[32] and were covalently attached to the Ge NWs using ethanedithiol as a molecular linker.[33] SEM images of the NWs after this attachment step are presented in Figure 2c and 2d and show complete coverage of Sn NPs on the surface of the Ge NWs. Si branch growth occurred via the vapor–liquid–solid (VLS) mechanism using the previously reported high boiling point solvent-vapor-growth system.[34,35] Briefly, the substrate was placed in the vapor zone of a high boiling point solvent and phenylsilane was injected into the reaction vessel at 460 °C. The Si branches grow in high density from the Ge NWs and have an average diameter of 14 nm (Figure 2e, f). The reaction temperature is well above the melting temperature of the NPs, ensuring that the melted Sn wets the surface of the Ge. This facilitates a good electrical contact between the Ge and the Si at the point of growth which is important for dual cycling of both the NW and the branch.[36]

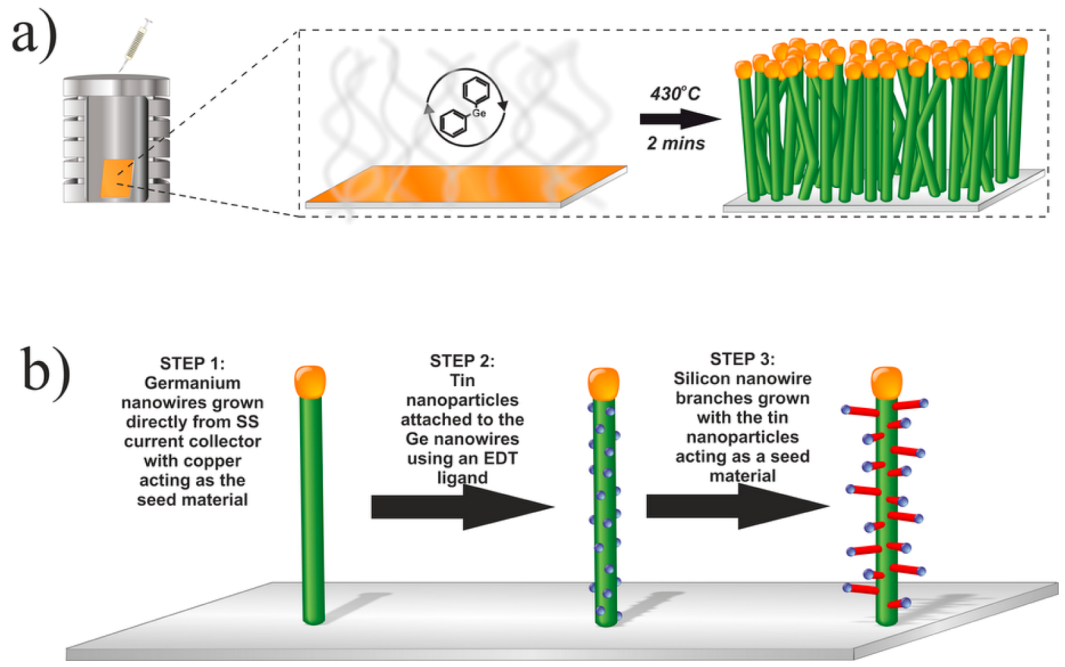

Figure 1. (a) Schematic illustrating the synthetic method used for Ge NW growth. The current collector, consisting of a 1 nm layer of Cu thermally evaporated onto a stainless steel substrate, is placed on the heat source and within a specially designed, hollowed out confiner. The temperature is ramped to 430 °C before injection of the germanium based precursor. Growth proceeds via the well-known VSS mechanism. (b) Schematic illustrating the synthetic protocol for Si NW branch growth. Sn NPs are attached to the surface of the Ge NWs using a molecular linker. The Sn NPs act as seeds for Si NW branch growth that occurs via the VLS mechanism in the vapor phase of a high boiling point solvent.

By varying the Si reaction time it was possible to control the Ge to Si mass ratio of the electrode with longer times resulting in a higher Si content. Further SEM analysis of the material at each stage of synthesis is presented in the Supporting Information (Figures S2 and S3). Scanning transmission electron microscopy (STEM) analysis of the branched NWs revealed the tendency of the branches to grow in a vinelike manner, wrapping around the NW and creating multiple contact points between the Si and the Ge (Figure 3a). Energy-dispersive X-ray spectroscopy (EDX) was employed to map Ge and Si in the heterostructure and is presented in Figure 3b with the elemental map for Si superimposed over the elemental map for Ge (the individual elemental maps are presented in the Supporting Information, Figure S4). The results show an almost core−shell-like structure similar to those previously reported[22] with the important distinction that the Ge NW is not constrained by the Si branches as in a typical core−shell nanowire. Previous reports on core−shell Si−Ge NWs have shown that there is an increased strain on the material during charging as a consequence of the higher lithiation potential of Ge over Si, limiting their cycle life and rate capability. This is avoided here as both the Ge NW and Si branch have the freedom to expand and contract without constraint during cycling.

Low resolution TEM analysis of a straight Ge NW (Figure 3c) also revealed the vinelike coverage of the Si branches. HRTEM images of the highlighted areas of the Ge NW and the Si branch are presented in Figure 3d and 3e, respectively. The straight Ge NW is single crystal and has a ⟨110⟩ growth direction, typically seen for Cu_3Ge-seeded NWs (Figure 3d). The inset fast Fourier transform (FFT) pattern is indexed with spots corresponding to the (111) and (113) planes, matching those expected for cubic Ge. The HRTEM image of the Si branch (Figure 3e) shows an FFT pattern indexed with spots corresponding to the (111) and (022) planes and is consistent with a ⟨111⟩ growth direction. X-ray diffraction (XRD) analysis (Figure 3f) of the as-synthesized material gave reflections consistent with cubic Ge and cubic Si (both with space group *Fd*−3*m*) with remaining peaks corresponding to the underlying SS. No peaks were identified for the c-Cu_3Ge and c-Sn seeds which was due to the comparatively low mass of each in the material.

Electrochemical Characterization of the Branched NW Heterostructures. The electrochemical properties of the branched NWs were tested by galvanostatic cycling in a two electrode Swagelok cell cycled in the voltage range of 0.01 to 1.0 V versus Li/Li^+ in a 1 M $LiPF_6$ in ethylene carbonate/diethyl carbonate (1:1 v/v) + 3 wt % vinylene carbonate (VC) electrolyte. By varying the time of the Si reaction it was possible to tune the composition of the material, with longer reaction times resulting in a higher mass ratio of Si. The electrochemical properties of three different Ge to Si mass ratios were evaluated, namely 2:1, 3:1 and 4:1 Ge to Si, with each having maximum theoretical specific capacities of 2115, 1933,

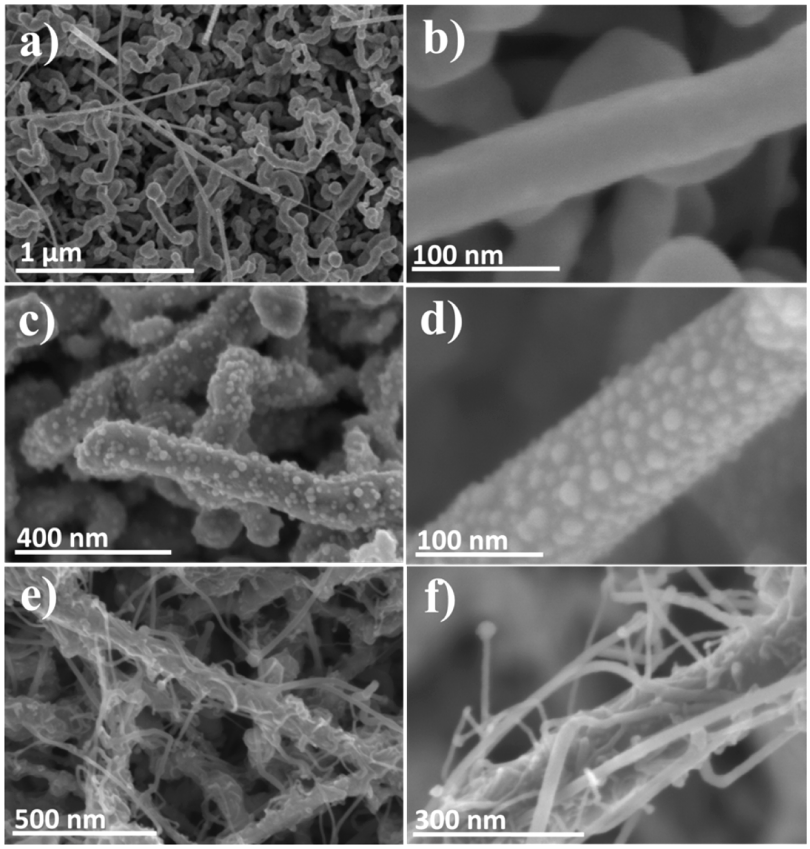

Figure 2. (a, b) Low and high magnification HRSEM images of as-synthesized Cu_3Ge seeded Ge NWs showing both straight and wormlike morphologies. (c, d) Low and high magnification HRSEM images of Ge NWs with Sn NPs attached to the surface. The NPs are attached using ethanedithiol as a molecular linker. (e, f) Low and high magnification HRSEM images of the Si NW branches growing in high density from the Ge NWs. Sn NPs act as seeds for Si branch growth.

and 1823 mAh/g, respectively. The masses of each component were obtained by carefully weighing each substrate at each stage of the reaction using an ultramicrobalance and were confirmed using EDX measurements (Supporting Information Figure S5). The compositions of all the electrodes tested in this study were within 5% of their given mass ratio. The as grown Si−Ge branched NW heterostructures on SS were used directly as the working electrode and the material was cycled at a C/5 rate for 100 cycles. The electrochemical processes occurring during charging and discharging were elucidated by plotting the differential capacity of the first and second cycles of each composition (Figure S6 a-c) and clearly show the dual cycling of both the Ge NW and the Si branch. The discharge capacities and Coulombic efficiencies (CE) for each composition cycled at a C/5 rate are shown in Figure 4a. The 2:1, 3:1, and 4:1 compositions exhibited initial discharge capacities of 1484, 1255, and 1249 mAh/g, respectively, which increased to 1777, 1550, and 1325 mAh/g over the early cycling period. This rise in capacity is due to the innate property of Si to only partially lithiate over the initial cycles forming a core−shell structure consisting of a c-Si core and a-$Li_{15}Si_4$ shell.[37−39] As cycling progresses the crystalline core decreases in diameter upon each subsequent full charge resulting in an increase in capacity, until eventually the fully charged NW consists completely of a-$Li_{15}Si_4$. The exhibited capacities are below the maximum theoretical specific capacity calculated for each composition which is more than likely a consequence of the existence of a native oxide layer on the material as the substrates were exposed to the atmosphere during washing and weighing steps.[40] The native oxide layers of both Ge and Si irreversibly alloy with Li leading to reduced capacities.[41] The material exhibited first cycle CE values of 65.8% (2:1), 68.1% (3:1), and 71.4% (4:1). As expected the composition with the highest Si content has the lowest initial CE as the Si branches will have a relatively thicker native oxide layer due to their narrower diameters. After 100 cycles the samples displayed capacities of 1612 mAh/g (2:1), 1459 mAh/g (3:1), and 1256 mAh/g (4:1) corresponding to a capacity retention in each case of 91.0%, 94.1%, and 94.8%, compared to 95.2% for a pure Ge NW electrode (Supporting Information Figure S7a). Significantly, the capacity retention of the branched NWs is considerably better than that of a pure Si NW electrode. This is evident from Figure 4b that shows the normalized capacity retention of the Si−Ge branched NW heterostructures plotted alongside the capacity retention of a Si NW electrode with no Ge present. The Si NWs on their own only retained 82.9% of their initial capacity after

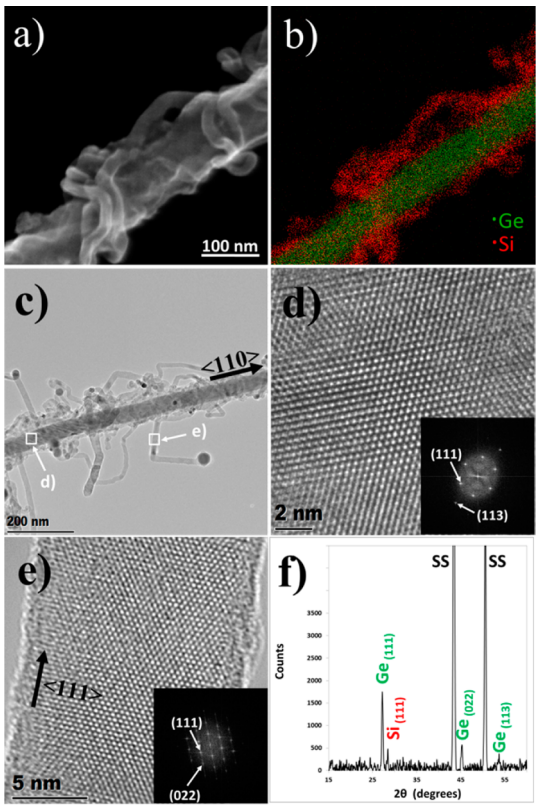

Figure 3. (a) STEM image of a Ge NW with Si branches. The branches grow in a vinelike manner around the Ge NW, creating multiple contact points between the two. (b) EDX elemental map showing signals from Ge (green) and from Si (red) overlaid. The material is similar to a core−shell-like structure with the distinction that the Si branches do not constrain the Ge NW during cycling. (c) TEM image of a Ge NW with Si branches growing in high density from it. (d) HRTEM image of the highlighted area of the ⟨110⟩ Ge NW in (c). The inset FFT is indexed with spots that correspond to cubic Ge. (e) HRTEM image of the highlighted area of the ⟨111⟩ Si branch in (c). The inset FFT is indexed with spots that correspond to cubic Si. (f) XRD pattern obtained from a Ge NW with Si branches substrate showing reflections corresponding to cubic Ge, cubic Si, and the SS current collector.

100 cycles, clearly illustrating the benefit of using Ge as a support structure for the cycling of Si.

The rate capability of the branched NWs was evaluated by charging and discharging the material for 5 cycles at rates of C/10, C/5, C/2, C, 2C, 5C, 10C, and then back to C/10 (Figure 4c). As a comparison the rate capability of a pure Si NW electrode was also tested using the same experimental procedure. As expected the electrodes with a higher Si content exhibited greater capacities at slower cycling rates due to the larger intrinsic capacity of Si. At cycling rates of C/10 and C/5 the pure Si electrode was the best performer exhibiting capacities of 2090 and 1936 mAh/g, respectively. However, as the cycling rates became more rapid, the composite electrodes began to outperform pure Si due to the greater electrical conductivity of Ge and its higher rate of Li^+ diffusivity.[26,27] At a cycling rate of C/2, the 2:1 Ge/Si composition performed equally as well as the Si electrode, both exhibiting capacities of ~1630 mAh/g, while at all rates above this it performed significantly better. A similar trend occurred for the other compositions with the 3:1 electrode performing equally as well or better than the Si electrode at rates of 1C and above and the 4:1 electrode outperforming the Si electrode at rates above 2C. All three branched NW electrodes displayed significantly higher capacities than Si at the two fastest rates with the 4:1 electrode in particular performing very well at the 10C rate, exhibiting a capacity of 802 mAh/g, over 6 times that of the pure Si electrode (130 mAh/g). The normalized capacity retention of the electrodes is presented in Figure 4d and clearly shows the branched NWs retain considerably more relative capacity at each cycle rate than Si. It is obvious from the graph that the higher the Ge content in the electrode the greater the relative capacity retention, which is again a consequence of the advantageous rate characteristics of Ge. This is also evident from analysis of the rate capability results of a pure Ge NW electrode wherein the Si-free material retains the highest relative capacity of all of the samples tested (Supporting Information Figure S7b,c). EIS measurements correlate well with these findings as they reveal that the impedance of the branched NW heterostructure electrodes increases with increasing Si content, explaining the inhibiting effect Si has on the rate capability (Supporting Information Figure S8). Overall these results demonstrate the benefit of using a multielement system as by simply controlling the Ge:Si mass ratio it is possible to tailor the properties of the electrode. This allows the material to be designed to meet specific requirements between the range of very high capacity at a low material cost (Si rich) or high rate capability and improved cycling stability at a higher material cost (Ge rich).

Effect of Cycling on the Material. The effect of cycling on the morphology of the heterostructure material was evaluated by an *ex situ* electron microscopy study. Figure 5 shows SEM and TEM images of the branched NWs (2:1 composition) after 100 cycles. We previously reported the cycling behavior of Ge in the presence of the electrolyte additive, VC, whereby the morphology of the NWs is completely restructured as a consequence of the charge/discharge process to form a spongelike, porous network of ligaments.[28] The formation of this network is linked to the fact that Ge NWs form nanopores upon delithiation and as Si NWs also form nanopores[42,43] due to cycling, it was anticipated that the Si branches would incorporate into this stable network of Ge in a similar fashion. The SEM and TEM images reveal that the branched NW morphology has been replaced by the network of ligaments with the active material agglomerating into islands that remain well contacted to the current collector (Figure 5a, b). The TEM images (Figure 5c, d) reveal the spongelike nature and porosity of the restructured active material which is highly advantageous as the empty space

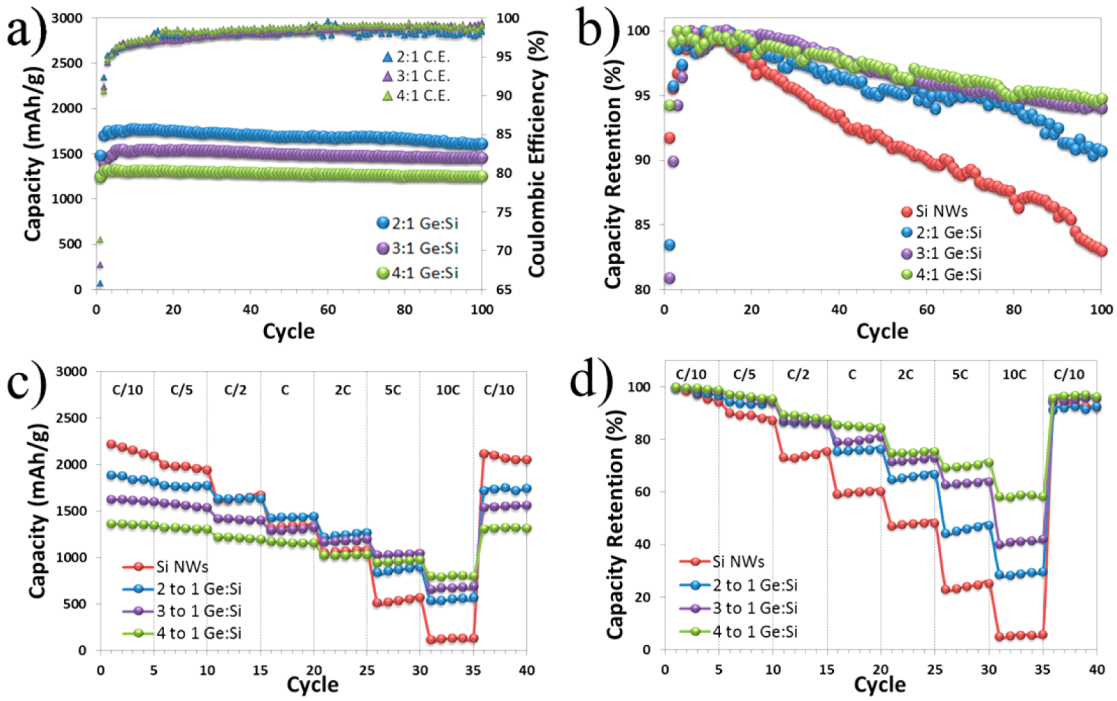

Figure 4. (a) Discharge capacities and Coulombic efficiencies over 100 cycles of the three different compositions of Si−Ge branched NW heterostructures. The active material was charged and discharged at a C/5 rate in the potential range of 0.01−1.0 V. (b) Relative capacity retention of the Ge NWs with Si branches over 100 cycles plotted alongside the relative capacity retention of Si NWs grown directly from a stainless steel current collector. (c) Discharge capacities at various cycling rates of each branched NW heterostructure composition and for a pure Si NW electrode are presented. All electrodes were charged and discharged for 5 cycles at each rate shown in the potential range of 0.01−1.0 V. All branched NW heterostructure electrodes show equal or higher capacities than Si at rates above 1C. (d) Normalized percent capacity retention of each branched NW heterostructure composition alongside that of a pure Si NW electrode are shown. All branched NW heterostructure electrodes retained a significantly higher amount of their original capacity at each rate than pure Si.

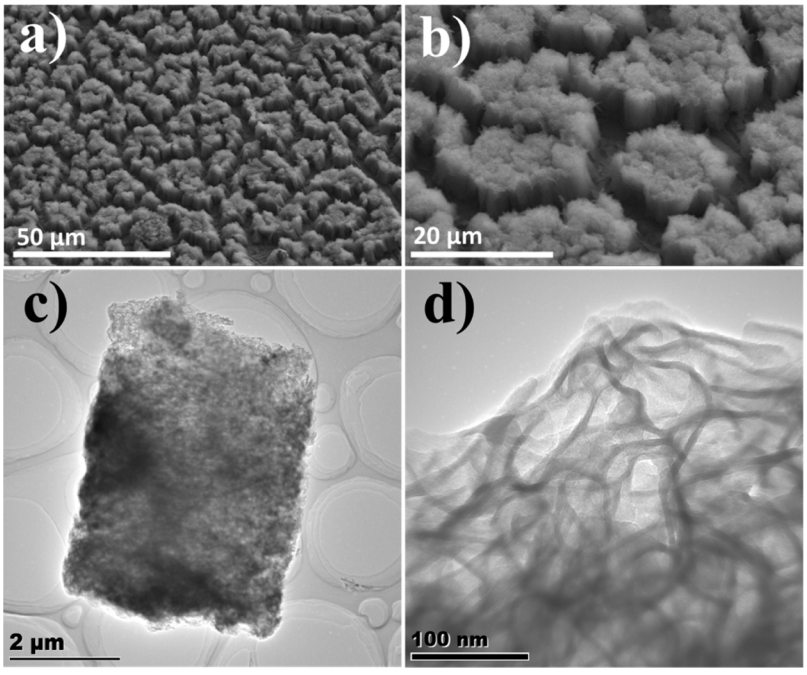

Figure 5. (a, b) Low and high magnification HRSEM images of the branched NW heterostructure electrodes after 100 cycles. The original NW morphology is completely lost as a result of cycling, having been replaced by a network of active material. The NWs agglomerate during network formation to create islands of active material across the substrate. (c) Low magnification HRTEM image of the active material after 100 cycles. The spongelike nature of the material is apparent. (d) High magnification HRTEM image of the network showing the network consists of interweaving ligaments of active material.

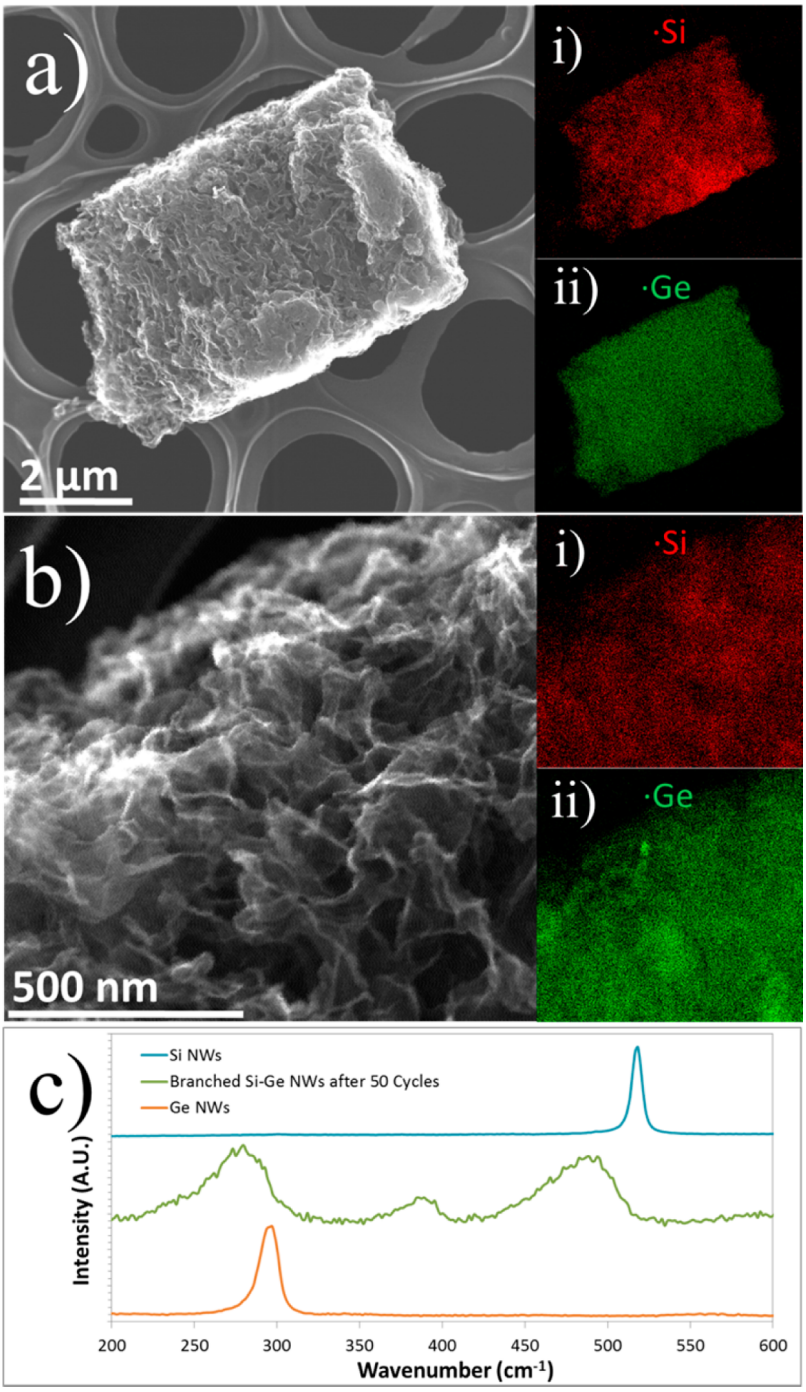

Figure 6. (a) Low magnification STEM image of the active material after 100 cycles. EDX elemental maps of (i) Si and (ii) Ge. The maps show a relatively even dispersion of both elements throughout the network. (b) High magnification STEM image of the active material after 100 cycles. EDX elemental maps of (i) Si and (ii) Ge. (c) Raman spectra of a branched heterostructure NW electrode after 50 cycles, a pristine Si NW electrode, and a pristine Ge NW electrode. As a result of cycling, the branched NW heterostructure electrode has transformed into a Si−Ge alloy.

can accommodate the volume changes associated with the charge/discharge processes, alleviating any stress build up that would otherwise be encountered by the material.

EDX mapping at low magnification (Figure 6a, i and ii) and high magnification (Figure 6b, i and ii) reveal a relatively even dispersion of both Si and Ge throughout the network. These results suggest that the restructuring process has transformed the material from a Si−Ge heterostructure into a $Si_{1-x}Ge_x$ alloy, most likely due a phenomenon known as lithium assisted, electrochemical welding.[44,45] Raman spectroscopy of the branched NW heterostructures after 100 cycles compared to a pure Si NW substrate and a pure Ge NW substrate (Figure 6c) confirmed this transformation. The peak sizes of Si and Ge have been normalized to the height of the signal from

the network. The Si NW substrate and Ge NW substrate show single, sharp peaks at 520 and 297 cm^{-1}, respectively, corresponding to c-Si and c-Ge. The Raman spectrum of the network after 100 cycles shows three broad peaks at 279, 387, and 489 cm^{-1} and is consistent with the spectrum of a Si–Ge alloy.[40,46] The transformation from heterostructure to alloy occurs as during lithiation Li atoms can bond simultaneously with Si and Ge at points of contact between the branch and the NW, creating a Si–Li–Ge bridge. During delithiation this link is broken creating a kinetic driving force for Si–Ge bond formation at the interface, having the overall effect of decreasing the surface energy of the material.[45] The vinelike manner of growth of the Si branches around the Ge NW is likely to be an advantageous property in this regard as the multiple contact points promote the fusion of Si and Ge through cycling, ultimately transforming the material from a Si–Ge heterostructure to a Si–Ge alloy network. It is believed that alloy formation has a positive impact on the capacity retention of the electrodes as it prevents detachment of the Si branches from the Ge NW stem in the initial cycles that could otherwise lead to loss of electrical contact and a reduction in capacity.

CONCLUSION

In summary, unique Si–Ge branched NW heterostructures were successfully grown from stainless steel current collectors using solvent-vapor growth systems. The Ge NWs were grown via a VSS mechanism using a low cost rapid pyrolysis synthetic protocol. The Si branches were synthesized via a secondary seeding method using Sn NPs and grew in high density from the Ge stem. The performances of three different Ge to Si mass ratios were investigated as possible anode materials for Li-ion batteries. The heterostructure electrodes exhibited high capacities and excellent capacity retention, retaining as much as ~95% after 100 cycles. The rate capability of the electrodes was also tested, and it was found that the more Ge rich the electrode the greater the capacity retention at high rates, while the more Si rich electrodes exhibited higher capacities at slower cycling rates. Through an *ex situ* study on the effect of cycling on the morphology of the electrodes, it was found that the branched NW heterostructures completely transformed into a porous, Si–Ge alloyed network. On the whole, we believe that the fabrication of the Si–Ge branched NW heterostructures to be a scalable method, and when used as a Li-ion battery anode they offer a viable alternative to conventional graphitic based electrodes. The rational design of the material provides an electrode with tunable properties, allowing the performance to be tailored for either high capacity or high rate capability depending on the power demands of the end application.

EXPERIMENTAL METHODS

Substrate Preparation. Stainless steel (SS, 316) foil was purchased from Pi-Kem Ltd. with a thickness of 0.1 mm and was untreated prior to use. Prior to treatment, the substrates were roughened using P600 grit sandpaper to increase the surface area and improve the contact between the active material and the current collector. A 1 nm layer of Cu (99.999%, Kurt J. Lesker) was then thermally evaporated onto the SS substrates in a glovebox-based evaporation unit. The substrates were stored in an Ar glovebox prior to reactions and contact with O_2 was minimized.

Chemicals Used. All chemicals were used as received. Diphenylgermane (DPG; 97%) was supplied by Gelest and was stored and dispensed from an Ar-filled glovebox. Phenylsilane (PS; 97%, Aldrich) was supplied by Sigma-Aldrich and was also stored and dispensed from an Ar-filled glovebox

Reaction Setup. *Ge NWs.* Reactions were carried out in an Ar-filled glovebox using a Stuart CD162 digital stirrer/hot plate with a maximum temperature of 450 °C. The pretreated SS current collectors were placed on the hot plate at 425 °C standing upright, and the temperature was allowed to equilibrate for 1 min prior to reaction. A SS confiner, specially designed to prevent the escape of the precursor vapor, was placed over the SS substrate and the appropriate volume (10 μL) of the DPG precursor was injected through a small hole in the top. The reaction was allowed to proceed for 2 min before removing the SS confiner allowing the vapor to escape, thus terminating the reaction. The electrodes had an average loading of Ge of 0.31 mg/cm^2.

Attachment of Sn NPs to Ge NWs. The Sn NPs were synthesized using a previously reported procedure.[32] The NPs were then washed, and a ligand exchange was performed using oleic acid. This was achieved by adding 1 mL of hexane, 1 mL of octadecene, and 5 drops of oleic acid to 1 mL of the Sn NP dark brown reaction mixture. The resulting mixture was mixed thoroughly using a vortex mixer. The solution was then allowed to settle into two separate layers. The bottom colorless layer was discarded and the brown top layer containing Sn nanoparticles was recovered. The procedure was repeated once more and the brown solution containing the Sn NPs was recovered and used without further purification.

The Sn NPs were covalently attached to the Ge NWs using ethanedithiol (EDT) as a molecular linker. This was achieved by immersing the Ge NW substrates in EDT for 1 h. The substrates were then taken out and rinsed with ACN, dried, and then immersed in the solution of Sn NPs solution for 24 h. The substrates were then washed thoroughly with hexane and dried with a nitrogen line.

Si Branch Growth. Reactions were carried out in custom-made Pyrex, round bottomed flasks. The Ge NW with Sn NPs substrates were placed vertically in the flask which was attached to a Schlenk line setup via a water condenser. A volume of 7 mL of squalane (99%, Aldrich) was added, and the system was then ramped to a temperature of 125 °C using a three zone furnace. A vacuum of at least 100 mTorr was applied for 1 h to remove moisture from the system. Following this, the system was purged with Ar. The flask was then ramped to the reaction temperature under a constant Ar flow.

Reactions were carried out at 460 °C. A water condenser was used to control the solvent reflux and ensure that the reaction was kept under control. At the correct reaction temperature, PS was injected through a septum cap into the system. Various reaction times were carried out to grow the different Ge:Si compositions used in the study. Reaction times of 45 min (4:1), 1 h (3:1), and 1.5 h (2:1) were found to be the optimum. To terminate the reaction, the furnace was opened and the setup was allowed to cool to room temperature before extracting the substrates.

Analysis. Scanning electron microscopy (SEM) analysis was performed on a Hitachi SU-70 system operating between

3 and 20 kV. The substrates were untreated prior to SEM analysis. For transmission electron microscopy (TEM) analysis, the branched NWs were removed from the growth substrate through sonication. TEM analysis was conducted using a 200 kV JEOL JEM-2100F field emission microscope equipped with a Gatan Ultrascan CCD camera and EDAX Genesis EDS detector. Electron dispersive X-ray (EDX) spectroscopy of the branched NWs was conducted on Au TEM grids. X-ray diffraction (XRD) analysis was conducted using a PANalytical X'Pert PRO MRD instrument with a Cu Kα radiation source (λ = 1.5418 Å) and an X'celerator detector. The mass of the each component of the branched NWs was determined through careful measurement using a Sartorius Ultra-Microbalance SE2 (repeatability $\pm$0.25 μg). Raman analysis was carried out on an inVia confocal Raman spectrophotometer (Renishaw) with an optical microscope interface (Leica). Samples were excited using a 532 nm laser at room temperature, and results were recorded at 0.1% power for 30 s.

Electrochemical Measurements. The electrochemical performance was evaluated by assembling two electrode Swagelok cells in an Ar filled glovebox. The cells consisted of Si−Ge branched NWs on SS substrates as the working electrode, Li foil as the counter and reference electrode, a Celgard separator, and an electrolyte solution of 1 M $LiPF_6$ in ethylene carbonate/diethyl carbonate (1:1 v/v) + 3 wt % vinylene carbonate. The measurements were carried out galvanostatically using a Biologic MPG-2 in the potential range of 0.01−1.0 V versus Li/Li^+. In the cases where Si only electrodes were used in the study, these were fabricated by a previously published procedure.[35]

Electrochemical Impedance Spectroscopy (EIS) was performed using the same type of working electrodes, separator, and electrolyte. However, a T-shaped, three-electrode Swagelok cell was used for these experiments, with separate counter and reference electrodes, each composed of Li foil. Data was collected using an Autolab PGSTAT100 potentiostat with a built-in FRA2 impedance module. Prior to measurement, the NW electrodes were subject to galvanostatic charge/discharge as described for the two electrode configuration, with discharge interrupted at 0.45 V on the second delithiation and the cell allowed to relax on open circuit until the magnitude of the potential drift fell below 1.0 mV/h. EIS spectra were then recorded in the absence of DC bias, with an applied AC perturbation of 10 mV peak amplitude, and a frequency range of 100 kHz to 5 mHz.

Conflict of Interest: The authors declare no competing financial interest.

Acknowledgment. This work was supported by Science Foundation Ireland (SFI) under the Principal Investigator Program under Contract No. 11PI-1148 and also by EU FP7 funding - GREENLION Project - Contract no. 285268. T.K. acknowledges Intel Ireland and the Irish Research Council for funding through the Enterprise Partnership Scheme. We gratefully acknowledge L. Kailas for carrying out the Raman spectroscopy measurements.

Supporting Information Available: Additional SEM images of the NWs at each stage of synthesis as well as a STEM image of a branched NW. Individual and combined EDX Si and Ge elemental maps, EDX spectra, and quantitative analysis showing mass ratios of the branched NWs, additional discussion on the phase changes occurring during cycling along with differential capacity plots of the first and second cycle of the branched NWs, cycling data and rate capability of the branched NWs compared to a pure Ge NW sample, and EIS measurements of the branched NW heterostructures with mass ratios of 2:1, 3:1 and 4:1. The Supporting Information is available free of charge on the ACS Publications website at DOI: 10.1021/acsnano.5b02528.

REFERENCES AND NOTES

1. Bogart, T. D.; Chockla, A. M.; Korgel, B. A. High Capacity Lithium Ion Battery Anodes of Silicon and Germanium. *Curr. Opin. Chem. Eng.* **2013**, *2*, 286–293. DOI: 10.1016/j.coche.2013.07.001.
2. Park, C.-M.; Kim, J.-H.; Kim, H.; Sohn, H.-J. Li-Alloy Based Anode Materials for Li Secondary Batteries. *Chem. Soc. Rev.* **2010**, *39*, 3115–3141. DOI: 10.1039/b919877f.
3. Su, X.; Wu, Q.; Li, J.; Xiao, X.; Lott, A.; Lu, W.; Sheldon, B. W.; Wu, J. Silicon-Based Nanomaterials for Lithium-Ion Batteries: A Review. *Adv. Energy Mater.* **2014**, *4*, 1300882. DOI: 10.1002/aenm.201300882.
4. Liu, Y.; Zhang, S.; Zhu, T. Germanium-Based Electrode Materials for Lithium-Ion Batteries. *ChemElectroChem* **2014**, *1*, 706–713. DOI: 10.1002/celc.201300195.
5. Choi, N.-S.; Yao, Y.; Cui, Y.; Cho, J. One Dimensional Si/Sn-Based Nanowires and Nanotubes for Lithium-Ion Energy Storage Materials. *J. Mater. Chem.* **2011**, *21*, 9825–9840. DOI: 10.1039/c0jm03842c.
6. Chan, C. K.; Peng, H.; Liu, G.; McIlwrath, K.; Zhang, X. F.; Huggins, R. A.; Cui, Y. High-Performance Lithium Battery Anodes Using Silicon Nanowires. *Nat. Nanotechnol.* **2008**, *3*, 31–35. DOI: 10.1038/nnano.2007.411.
7. Chockla, A. M.; Harris, J. T.; Akhavan, V. A.; Bogart, T. D.; Holmberg, V. C.; Steinhagen, C.; Mullins, C. B.; Stevenson, K. J.; Korgel, B. A. Silicon Nanowire Fabric as a Lithium Ion Battery Electrode Material. *J. Am. Chem. Soc.* **2011**, *133*, 20914–20921. DOI: 10.1021/ja208232h.
8. Chockla, A. M.; Klavetter, K. C.; Mullins, C. B.; Korgel, B. A. Solution-Grown Germanium Nanowire Anodes for Lithium-Ion Batteries. *ACS Appl. Mater. Interfaces* **2012**, *4*, 4658–4664. DOI: 10.1021/am3010253.
9. Chockla, A. M.; Klavetter, K.; Mullins, C. B.; Korgel, B. A. Tin-Seeded Silicon Nanowires for High Capacity Li-Ion Batteries. *Chem. Mater.* **2012**, *24*, 3738–3745. DOI: 10.1021/cm301968b.
10. Geaney, H.; Kennedy, T.; Dickinson, C.; Mullane, E.; Singh, A.; Laffir, F.; Ryan, K. M. High Density Growth of Indium Seeded Silicon Nanowires in the Vapor Phase of a High Boiling Point Solvent. *Chem. Mater.* **2012**, *24*, 2204–2210. DOI: 10.1021/cm301023j.
11. Kim, H.; Cho, J. Superior Lithium Electroactive Mesoporous Si@Carbon Core−Shell Nanowires for Lithium Battery Anode Material. *Nano Lett.* **2008**, *8*, 3688–3691. DOI: 10.1021/nl801853x.
12. Yuan, F.-W.; Yang, H.-J.; Tuan, H.-Y. Alkanethiol-Passivated Ge Nanowires as High-Performance Anode Materials for Lithium-Ion Batteries: The Role of Chemical Surface Functionalization. *ACS Nano* **2012**, *6* (11), 9932–9942. DOI: 10.1021/nn303519g.
13. Chan, C. K.; Zhang, X. F.; Cui, Y. High Capacity Li Ion Battery Anodes Using Ge Nanowires. *Nano Lett.* **2008**, *8*, 307–309. DOI: 10.1021/nl0727157.
14. Ko, Y.-D.; Kang, J.-G.; Lee, G.-H.; Park, J.-G.; Park, K.-S.; Jin, Y.-H.; Kim, D.-W. Sn-Induced Low-Temperature Growth of Ge Nanowire Electrodes with a Large Lithium Storage Capacity. *Nanoscale* **2011**, *3*, 3371–3375. DOI: 10.1039/c1nr10471c.
15. Cui, L.-F.; Yang, Y.; Hsu, C.-M.; Cui, Y. Carbon−Silicon Core−Shell Nanowires as High Capacity Electrode for Lithium Ion Batteries. *Nano Lett.* **2009**, *9*, 3370–3374. DOI: 10.1021/nl901670t.
16. Cui, L.-F.; Ruffo, R.; Chan, C. K.; Peng, H.; Cui, Y. Crystalline-Amorphous Core− Shell Silicon Nanowires for High Capacity and High Current Battery Electrodes. *Nano Lett.* **2009**, *9*, 491–495. DOI: 10.1021/nl8036323.
17. Memarzadeh Lotfabad, E.; Kalisvaart, P.; Cui, K.; Kohandehghan, A.; Kupsta, M.; Olsen, B.; Mitlin, D. Ald TiO_2 Coated Silicon Nanowires for Lithium Ion Battery Anodes with Enhanced Cycling Stability and Coulombic Efficiency. *Phys. Chem. Chem. Phys.* **2013**, *15*, 13646–13657. DOI: 10.1039/c3cp52485j.
18. Chen, H.; Xiao, Y.; Wang, L.; Yang, Y. Silicon Nanowires Coated with Copper Layer as Anode Materials for Lithium-Ion Batteries. *J. Power Sources* **2011**, *196*, 6657–6662. DOI: 10.1016/j.jpowsour.2010.12.075.
19. Cho, J.-H.; Picraux, S. T. Enhanced Lithium Ion Battery Cycling of Silicon Nanowire Anodes by Template Growth to Eliminate Silicon Underlayer Islands. *Nano Lett.* **2013**, *13*, 5740–5747. DOI: 10.1021/nl4036498.

20. Esmanski, A.; Ozin, G. A. Silicon Inverse-Opal-Based Macroporous Materials as Negative Electrodes for Lithium Ion Batteries. *Adv. Funct. Mater.* **2009**, *19*, 1999–2010. DOI: 10.1002/adfm.200900306.
21. Hu, Y. S.; Demir-Cakan, R.; Titirici, M. M.; Müller, J. O.; Schlögl, R.; Antonietti, M.; Maier, J. Superior Storage Performance of a Si@ SiO_x/C Nanocomposite as Anode Material for Lithium-Ion Batteries. *Angew. Chem., Int. Ed.* **2008**, *47*, 1645–1649. DOI: 10.1002/anie.200704287.
22. Song, T.; Cheng, H.; Town, K.; Park, H.; Black, R. W.; Lee, S.; Park, W. I.; Huang, Y.; Rogers, J. A.; Nazar, L. F.; et al. Electrochemical Properties of Si-Ge Heterostructures as an Anode Material for Lithium Ion Batteries. *Adv. Funct. Mater.* **2014**, *24*, 1458–1464. DOI: 10.1002/adfm.201302122.
23. Song, T.; Cheng, H.; Choi, H.; Lee, J.-H.; Han, H.; Lee, D. H.; Yoo, D. S.; Kwon, M.-S.; Choi, J.-M.; Doo, S. G.; et al. Si/Ge Double-Layered Nanotube Array as a Lithium Ion Battery Anode. *ACS Nano* **2012**, *6*, 303–309. DOI: 10.1021/nn203572n.
24. Wang, J.; Du, N.; Zhang, H.; Yu, J.; Yang, D. Cu−Si 1− X Ge X Core−Shell Nanowire Arrays as Three-Dimensional Electrodes for High-Rate Capability Lithium-Ion Batteries. *J. Power Sources* **2012**, *208*, 434–439. DOI: 10.1016/j.jpowsour.2012.02.039.
25. Li, J.; Dudney, N. J.; Xiao, X.; Cheng, Y.-T.; Liang, C.; Verbrugge, M. W. Asymmetric Rate Behavior of Si Anodes for Lithium-Ion Batteries: Ultrafast De-Lithiation *Versus* Sluggish Lithiation at High Current Densities. *Adv. Energy Mater.* **2015**, *5*, 1401627. DOI: 10.1002/aenm.201401627.
26. Graetz, J.; Ahn, C.; Yazami, R.; Fultz, B. Nanocrystalline and Thin Film Germanium Electrodes with High Lithium Capacity and High Rate Capabilities. *J. Electrochem. Soc.* **2004**, *151*, A698–A702. DOI: 10.1149/1.1697412.
27. Wang, D.; Chang, Y.-L.; Wang, Q.; Cao, J.; Farmer, D. B.; Gordon, R. G.; Dai, H. Surface Chemistry and Electrical Properties of Germanium Nanowires. *J. Am. Chem. Soc.* **2004**, *126*, 11602–11611. DOI: 10.1021/ja047435x.
28. Kennedy, T.; Mullane, E.; Geaney, H.; Osiak, M.; O'Dwyer, C.; Ryan, K. M. High-Performance Germanium Nanowire-Based Lithium-Ion Battery Anodes Extending over 1000 Cycles Through *In Situ* Formation of a Continuous Porous Network. *Nano Lett.* **2014**, *14*, 716–723. DOI: 10.1021/nl403979s.
29. Mullane, E.; Kennedy, T.; Geaney, H.; Ryan, K. M. A Rapid, Solvent-Free Protocol for the Synthesis of Germanium Nanowire Lithium-Ion Anodes with a Long Cycle Life and High Rate Capability. *ACS Appl. Mater. Interfaces* **2014**, *6*, 18800–18807. DOI: 10.1021/am5045168.
30. Geaney, H.; Mullane, E.; Ryan, K. M. Solution Phase Synthesis of Silicon and Germanium Nanowires. *J. Mater. Chem. C* **2013**, *1*, 4996–5007. DOI: 10.1039/c3tc31123f.
31. Bezuidenhout, M.; Kennedy, T.; Belochapkine, S.; Guo, Y.; Mullane, E.; Kiely, P. A.; Ryan, K. M. High Density and Patternable Growth of Silicon, Germanium and Alloyed SiGe Nanowires by a Rapid Anneal Protocol. *J. Mater. Chem. C* **2015**, . DOI: 10.1039/C5TC01389E.
32. Jo, Y. H.; Jung, I.; Choi, C. S.; Kim, I.; Lee, H. M. Synthesis and Characterization of Low Temperature Sn Nanoparticles for the Fabrication of Highly Conductive Ink. *Nanotechnology* **2011**, *22*, 225701. DOI: 10.1088/0957-4484/22/22/225701.
33. Yu, W.; Isimjan, T.; Lin, B.; Takanabe, K. Surface Modification-A Novel Way of Attaching Cocatalysts on Cds Semiconductors for Photocatalytic Hydrogen Evolution. *IOP Conf. Ser.: Mater. Sci. Eng.* **2014**, 012057. DOI: 10.1088/1757-899X/64/1/012057.
34. Barrett, C. A.; Geaney, H.; Gunning, R. D.; Laffir, F. R.; Ryan, K. M. Perpendicular Growth of Catalyst-Free Germanium Nanowire Arrays. *Chem. Commun.* **2011**, *47*, 3843–3845. DOI: 10.1039/c0cc05202g.
35. Mullane, E.; Kennedy, T.; Geaney, H.; Dickinson, C.; Ryan, K. M. Synthesis of Tin Catalyzed Silicon and Germanium Nanowires in a Solvent−Vapor System and Optimization of the Seed/Nanowire Interface for Dual Lithium Cycling. *Chem. Mater.* **2013**, *25*, 1816–1822. DOI: 10.1021/cm400367v.
36. Geaney, H.; Mullane, E.; Ramasse, Q. M.; Ryan, K. M. Atomically Abrupt Silicon−Germanium Axial Heterostructure Nanowires Synthesized in a Solvent Vapor Growth System. *Nano Lett.* **2013**, *13*, 1675–1680. DOI: 10.1021/nl400146u.
37. Liu, X. H.; Zhang, L. Q.; Zhong, L.; Liu, Y.; Zheng, H.; Wang, J. W.; Cho, J.-H.; Dayeh, S. A.; Picraux, S. T.; Sullivan, J. P.; et al. Ultrafast Electrochemical Lithiation of Individual Si Nanowire Anodes. *Nano Lett.* **2011**, *11*, 2251–2258. DOI: 10.1021/nl200412p.
38. Zamfir, M. R.; Nguyen, H. T.; Moyen, E.; Lee, Y. H.; Pribat, D. Silicon Nanowires for Li-Based Battery Anodes: A Review. *J. Mater. Chem. A* **2013**, *1*, 9566–9586. DOI: 10.1039/c3ta11714f.
39. Liu, X. H.; Fan, F.; Yang, H.; Zhang, S.; Huang, J. Y.; Zhu, T. Self-Limiting Lithiation in Silicon Nanowires. *ACS Nano* **2013**, *7*, 1495–1503. DOI: 10.1021/nn305282d.
40. Abel, P. R.; Chockla, A. M.; Lin, Y.-M.; Holmberg, V. C.; Harris, J. T.; Korgel, B. A.; Heller, A.; Mullins, C. B. Nanostructured $Si_{(1-x)}Ge_x$ for Tunable Thin Film Lithium-Ion Battery Anodes. *ACS Nano* **2013**, *7*, 2249–2257. DOI: 10.1021/nn3053632.
41. McDowell, M. T.; Lee, S. W.; Ryu, I.; Wu, H.; Nix, W. D.; Choi, J. W.; Cui, Y. Novel Size and Surface Oxide Effects in Silicon Nanowires as Lithium Battery Anodes. *Nano Lett.* **2011**, *11*, 4018–4025. DOI: 10.1021/nl202630n.
42. Choi, J. W.; McDonough, J.; Jeong, S.; Yoo, J. S.; Chan, C. K.; Cui, Y. Stepwise Nanopore Evolution in One-Dimensional Nanostructures. *Nano Lett.* **2010**, *10*, 1409–1413. DOI: 10.1021/nl100258p.
43. Ogata, K.; Salager, E.; Kerr, C. J.; Fraser, A. E.; Ducati, C.; Morris, A. J.; Hofmann, S.; Grey, C. P. Revealing Lithium−Silicide Phase Transformations in Nano-Structured Silicon-Based Lithium Ion Batteries *via In Situ* NMR Spectroscopy. *Nat. Commun.* **2014**, *5*, 3217. DOI: 10.1038/ncomms4217.
44. Courtney, I. A.; McKinnon, W.; Dahn, J. On the Aggregation of Tin in SnO Composite Glasses Caused by the Reversible Reaction with Lithium. *J. Electrochem. Soc.* **1999**, *146*, 59–68. DOI: 10.1149/1.1391565.
45. Karki, K.; Epstein, E.; Cho, J.-H.; Jia, Z.; Li, T.; Picraux, S. T.; Wang, C.; Cumings, J. Lithium-Assisted Electrochemical Welding in Silicon Nanowire Battery Electrodes. *Nano Lett.* **2012**, *12*, 1392–1397. DOI: 10.1021/nl204063u.
46. Sui, Z.; Burke, H. H.; Herman, I. P. Raman Scattering in Germanium-Silicon Alloys Under Hydrostatic Pressure. *Phys. Rev. B: Condens. Matter Mater. Phys.* **1993**, *48*, 2162. DOI: 10.1103/PhysRevB.48.2162.